Direct method for imaging elemental distribution profiles with long-period x-ray standing waves

Vaibhav Kohli,[1,2] Michael J. Bedzyk,[1,3] and Paul Fenter[2]
[1]*Department of Materials Science and Engineering, Northwestern University, Evanston, Illinois 60208, USA*
[2]*Chemical Sciences and Engineering Division, Argonne National Laboratory, Argonne, Illinois 60439, USA*
[3]*Materials Science Division, Argonne National Laboratory, Argonne, Illinois 60439, USA*
(Received 14 October 2009; revised manuscript received 14 January 2010; published 19 February 2010)

A model-independent Fourier-inversion method for imaging elemental profiles from multilayer and total-external reflection x-ray standing wave (XSW) data is developed for the purpose of understanding the assembly of atoms, ions, and molecules at well-defined interfaces in complex environments. The direct-method formalism is derived for the case of a long-period XSW generated by low-angle specular reflection in an attenuating overlayer medium. It is validated through comparison with simulated and experimental data to directly obtain an elemental distribution contained within the overlayer. We demonstrate this formalism by extracting the one-dimensional profile of Ti normal to the surface for a TiO_2/Si/Mo trilayer deposited on a Si substrate using the Ti $K\alpha$ fluorescence yield measured in air and under an aqueous electrolyte. The model-independent results demonstrate reduced coherent fractions for the *in situ* results associated with an incoherency of the x-ray beam (which are attributed to fluorescence excitation by diffusely or incoherently scattered x-rays). The uniqueness and limitations of the approach are discussed.

DOI: 10.1103/PhysRevB.81.054112 PACS number(s): 61.05.cc, 68.08.De, 68.49.Uv

I. INTRODUCTION

Since the first demonstration that x-ray standing waves (XSW) can be used to determine the location of impurity atoms in single crystals,[1] the technique has been applied to measure the distribution of specific elements near or within complex structures including synthetic[2,3] and natural crystals,[4,5] surfaces,[6–9] thin films[10] and multilayers,[11–14] and fluid-crystal interfaces.[15–17] The target atomic species are selected via characteristic x-ray fluorescence (XRF) or photoelectron or Auger signals. XSW has been utilized in various configurations including diffraction from bulk crystals (Bragg single-crystal XSW or Bragg-XSW),[1–4,6,15,18–21] total-external reflection from x-ray mirrors (TR or TER XSW),[22–24] and reflection from periodic multilayer (PML XSW).[11–14,25] These techniques have differing sensitivities and strengths. For Bragg-XSW, the XSW period is defined by the diffraction-plane spacing (d). As such, it is ideal for locating elemental structures and distributions that are correlated with the substrate lattice with sub-Angstrom resolution. When applied to interfaces, it is most readily used to probe distributions that occur at heights (h) within one lattice spacing of the surface because of the modulo-d ambiguity[6,25] arising from the fact that the measurements are made only at the Bragg diffraction condition defined by the substrate crystal lattice. As shown recently for the case of self-assembled monolayers with $h > d$, x-ray reflectivity can be used to remove this modulo-d ambiguity from the XSW results.[26] At much smaller incident angles (θ), the TER and PML cases generate a so-called "long-period" XSW with a period $D = \lambda/(2 \sin \theta)$ that is much longer and varies continuously with incident angle, thereby providing sensitivity to extended elemental one-dimensional (1D) distributions that are much broader and are located further above the reflecting surface.

Analysis of XSW data has traditionally relied on model-dependent approaches. That is, the predictions of parameterized models of the elemental distribution were used to explain the observed fluorescence yield modulation. In the case of single-crystal Bragg-XSW, it was shown that the phase of the XSW corresponds to the phase of the structure factor of the diffracting crystal at the momentum transfer of the Bragg reflection condition.[18] The amplitude and phase of a Fourier coefficient of XRF-selected atomic density (i.e., the coherent fraction and coherent position of the element of interest) were shown to be obtained directly from a measured fluorescence yield modulation.[8,20] Comparison of these measured amplitudes and phases with the model-calculated values for different $H=hkl$ reflections allows the structure to be determined. For the long-period XSW, model-calculated fluorescence yields are typically compared with experimental data and fit through least-squares approaches. In all cases, the comparison between data and model-calculations is done after the x-ray reflectivity data are analyzed so that the XSW electric field intensity is known.

While the phase sensitivity of XSW data has been long acknowledged, it was demonstrated only recently[19] that elemental distributions can be obtained directly from the experimental Bragg-XSW data through a fully model-independent analysis. Here, we define a "model-independent" XSW analysis to be one in which an "image" of the elemental distribution can be obtained directly from the measured fluorescence yield data without using a parameterized model of the elemental structure in fitting the data (since model-based approaches have built-in assumptions about the elemental distribution). This model-independent XSW analysis is done after the total electron-density profile is known from a separate analysis of the x-ray reflectivity data. In the case of Bragg-XSW, the image of the elemental distribution is obtained by discrete Fourier inversion of the set of hkl Fourier amplitudes and phases obtained from each Bragg reflection. This was shown for the case of impurity atom distributions within a crystal[19] as well as for species located above the crystal surface.[26–29] This model-independent XSW analysis has only been applied to single-

crystal Bragg-XSW measurements. Recently Bedzyk demonstrated a different model-independent approach that is applicable to the TER-XSW regime.[24] Specifically, he showed that the fluorescence yield measured near the substrate critical angle can be converted to a modified yield whose inverse Fourier transform directly recovers the elemental distribution of interest. This approach is limited to the TER-XSW regime because it assumes that the phase of the reflected wave that participates in XSW varies linearly with scattering angle. Nevertheless, it shows that such model-independent approaches are applicable, in principle, to the long-period XSW regime.

Here we describe a generalized model-independent method for reconstructing elemental distribution profiles from XSW data. This approach is valid for the long-period XSW including TER and PML regimes. It also explicitly includes absorption so that it is applicable both within a material and above a reflecting surface. This approach makes use of the known complex reflectivity coefficients (determined from a separate analysis of the x-ray reflectivity data) and assumes that the element-specific partial structure factor varies slowly with momentum transfer, Q, so that the fluorescence yield variation within a given Q interval, $|Q-Q^0| < \Delta Q/2$ (where Q^0 and ΔQ are the center and width of the Q interval, respectively), can be described by a fixed amplitude, $A(Q^0)$, and phase, $P(Q^0)$, of the element-specific partial structure factor for that Q interval. When this condition is not satisfied, we show how the amplitude and phase variation within a given interval can be described by a linear Taylor-series expansion. The formalism allows the reconstruction of the elemental distribution directly by a simple Fourier transform using the complementary relationship between the elemental structure factor, $F(Q)=A(Q)\exp[i2\pi P(Q)]$, and the elemental density profile, $\rho(z)$ (where z denotes the vertical position)

$$\rho(z) = \frac{1}{2\pi}\int_{-\infty}^{+\infty} F(Q)\exp(-iQz)dQ. \tag{1}$$

This model-independent approach is applied to analyze Ti $K\alpha$ yield for a trilayer system consisting of a TiO_2 thin film grown on a Si/Mo bilayer on a Si substrate with the sample in air (*ex situ*) and in contact with an aqueous solution (*in situ*).

II. MODEL-INDEPENDENT METHOD

We first begin with a generalized description of XSW in an absorbing medium. When an x-ray plane wave is reflected from an interface between any two media, a standing wave is formed (Fig. 1) as a result of the superposition of the incident and reflected electric field (E field) plane waves. In the case where medium 1 is a vacuum layer, with refractive index $n_1=1$, consider the interface between two absorbing and refracting media, 2 and 3 with refractive indices n_2 and n_3, where $n_j=1-\delta_j-i\beta_j$. X-rays reflected from interface 2,3 (referred to as "the interface" in this derivation) result in a standing wave formation inside medium 2. The total E field inside medium 2 can be written as

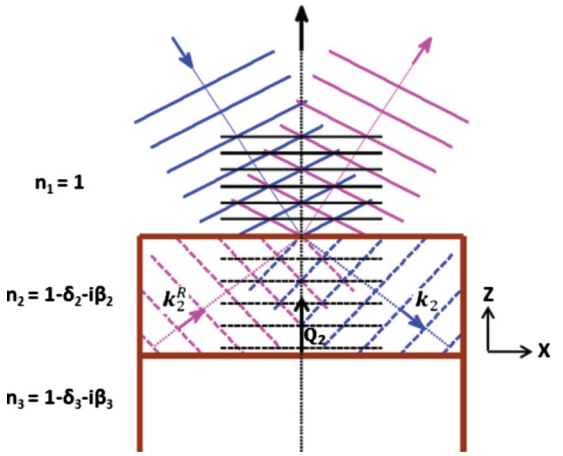

FIG. 1. (Color online) Reflection and refraction of x-ray beam at a vacuum-solid interface. The case shown is of a film (refractive index n_2) on a substrate (refractive index n_3), present in air ($n_1=1$). The incident and reflected waves are shown (in blue and magenta, respectively), along with the x-ray standing wave antinodes (horizontal black lines). The XSW is also generated within the film because of the presence of the reflection from the film-substrate interface ($\mathbf{k}_2$ and $\mathbf{k}_2^R$ denote the transmitted and reflected wave vectors inside the film). The effect due to refraction is exaggerated for clarity.

$$\boldsymbol{\varepsilon}_2^T(\mathbf{r},t) = \boldsymbol{\varepsilon}_2(\mathbf{r},t) + \boldsymbol{\varepsilon}_2^R(\mathbf{r},t) = \mathbf{E}_2\exp\{-i(\mathbf{k}_2\cdot\mathbf{r}-\omega t)\} + \mathbf{E}_2^R\exp\{-i(\mathbf{k}_2^R\cdot\mathbf{r}-\omega t)\}, \tag{2}$$

where $\mathbf{E}_2$ and $\mathbf{E}_2^R$ denote, respectively, the complex amplitudes of the incident and reflected E fields just above interface 2,3 (at $z=0$), and $\mathbf{k}_2$ and $\mathbf{k}_2^R$ denote the incident and reflected wave vectors, respectively. (We assume that the E fields are polarized perpendicular to the scattering plane, which is the *xz plane* in Fig. 1). The magnitude of both wave vectors is $k_2=\frac{2\pi}{\lambda}(1-\delta_2-i\beta_2)$. If R_2 is the magnitude squared and v_2 the phase of the reflectivity coefficient (E_2^R/E_2), at interface 2,3, we have

$$\boldsymbol{\varepsilon}_2^T(\mathbf{r},t) = \mathbf{E}_2\exp\{-i(\mathbf{k}_2\cdot\mathbf{r}-\omega t)\}\times[1+\sqrt{R_2}\exp(iv_2)\exp(-i\mathbf{Q}_2\cdot\mathbf{r})], \tag{3}$$

where $\mathbf{Q}_2=\mathbf{k}_2^R-\mathbf{k}_2$ is the wave-vector transfer in the medium 2. By the law of reflection, $\mathbf{Q}_2$ is oriented along the surface normal direction, and $\mathbf{Q}_2.\mathbf{r}=Q_2z$, where z is the height above interface 2,3. The complex quantity Q_2 is described in terms of a real and imaginary component as, $Q_2=Q_2'-iQ_2''$. The total E-field intensity in medium 2, normalized to the incident E-field intensity in vacuum, can now be written as

$$I_2(Q_2,z) = \frac{|\varepsilon_2^T|^2}{|E_1|^2} = \frac{|E_2(Q_2)|^2}{|E_1|^2}\exp(+Q_2''z)[1+R_2\exp(-2Q_2''z) + 2\sqrt{R_2}\exp(-Q_2''z)\cos(v_2-Q_2'z)]. \tag{4}$$

Here the factor $\exp(+Q_2''z)$ represents the attenuation of the incident wave in medium 2 that includes both the linear absorption as well as extinction (i.e., attenuation of the evanescent wave that occurs for incident angles below the critical

angle). Therefore Q_2'' is an effective linear absorption coeffi*cient. The prefactor representing the E-field intensity at $z=0$ just above interface 2,3 is obtained from the relation

$$|E_2(Q_2)|^2 = |E_1|^2|T_{1,2}|^2\exp(-Q_2''t_2), \tag{5}$$

where t_2 is the thickness of medium 2, and, $T_{1,2}$ is the transmission coefficient at the vacuum/medium-2 interface which is based on a modified Parratt's formalism described in detail elsewhere.[24,30,31] Specifically

$$T_{1,2} = \frac{1+F_{1,2}}{1+(F_{1,2})(E_2^R/E_2)\exp(-iQ_2t_2)}, \tag{6}$$

where $F_{1,2}$ is the Fresnel reflection coefficient of the interface 1,2 (i.e., ignoring the presence of any layers below layer 2), and E_2^R/E_2 is the Parratt's reflection coefficient of interface 2,3 (i.e., including all contributions from deeper layers). In these calculations, we have used a modified Fresnel reflection coefficient that includes the effect of interfacial roughness as a Debye-Waller factor multiplied to the original Fresnel-reflection coefficient.[30] Setting $|E_1|^2=1$, we obtain the normalized E-field intensity at any height z within medium-2 as

$$I_2(Q_2,z) = |E_2(Q_2)|^2[\exp(+Q_2''z) + R_2\exp(-Q_2''z) + 2\sqrt{R_2}\cos(v_2 - Q_2'z)]. \tag{7}$$

The first exponential term in the above equation represents the attenuation of the incident beam, the positive sign denotes that the beam is attenuated with *decreasing* height above the interface. The second exponential represents the attenuation of the reflected beam, which is attenuated with increasing height above the interface. The third term which is a result of coherent interference between the incident and reflected waves only has a z-independent attenuation in the medium.

We now derive an expression for the element-specific fluorescence yield. Based on the dipole approximation for the photoelectric effect, the fluorescence yield from an element with distribution $\rho(z)$ within medium 2 is given by

$$Y(Q_2) = \int_{z=0}^{t_2}\rho(z)I_2(Q_2,z)dz, \tag{8}$$

Here it is assumed that the effective absorption length in medium-2 for the emitted fluorescence x-ray is much larger than $\frac{t_2}{\sin(\alpha)}$, where α is the fluorescence emission take-off angle. Substitution of the Eq. (7) into the above expression and expanding the cosine term yields

$$Y(Q_2) = |E_2(Q_2)|^2[Y_0(Q_2) + R_2(Q_2)Y_0(-Q_2) + \sqrt{R_2(Q_2)}\{F^{*}\times(Q_2)\exp(iv_2) + F(Q_2)\exp(-iv_2)\}]. \tag{9}$$

The first term in the equation above, $Y_0(Q_2)=\int_{z=0}^{t_2}\rho(z)\exp(+Q_2''z)dz$, is the yield due to the incident beam only, i.e., the yield when $R=0$. And here

$$F(Q_2) \equiv \int_{z=0}^{t_2}\rho(z)\exp(iQ_2'z)dz = \rho^{2D}A(Q_2)\exp\{i2\pi P(Q_2)\} \tag{10}$$

is the structure factor (or Fourier transform) of the XRF-selected elemental distribution, $P(Q_2)$ the phase of the structure factor, and $A(Q_2)$ the amplitude of the normalized structure factor $F(Q_2)/\rho^{2D}$. Here $\rho^{2D}=\int_{z=0}^{t_2}\rho(z)dz$ is the two-dimensional (2D) atom number density of the fluorescing species, also referred to as the total coverage. The yield can be normalized to ρ^{2D}

$$\frac{Y(Q_2)}{\rho^{2D}} = |E_2(Q_2)|^2\left[\frac{Y_0(Q_2)}{\rho^{2D}} + R_2(Q_2)\frac{Y_0(Q_2)}{\rho^{2D}} + 2\sqrt{R_2(Q_2)}A(Q_2)\cos\{v_2(Q_2) - 2\pi P(Q_2)\}\right]. \tag{11}$$

We now consider two cases of interest in which the above expression can be simplified that allow for a straightforward model-independent analysis [i.e., allow $A(Q)$ and $P(Q)$ to be determined]. The first is a limiting case of a narrow distribution with an average height, z_0, above the interface 2,3, and distribution width, Δz. When $\Delta z \ll 1/Q_2''$, (the effective absorption length), the variation in the attenuating exponential factor in the expression for $Y_0(Q_2)$, over the range of Δz can be neglected (making this attenuation term dependent only on z_0), to obtain

$$\frac{Y(Q_2)}{\rho^{2D}} \cong |E_2(Q_2)|^2[\exp(+Q_2''z_0) + R_2(Q_2)\exp(-Q_2''z_0) + 2\sqrt{R_2(Q_2)}A(Q_2)\cos\{v_2(Q_2) - 2\pi P(Q_2)\}]. \tag{12}$$

Here the center of the distribution, z_0, is an unknown quantity, along with A and P, which can be determined from the analysis of the $Y(Q_2)$ data, as illustrated later in this paper. We also note that $z_0=2\pi P(Q_2)/Q_2$ in the limit of $Q_2\to 0$.

Another limiting case for Eq. (11) is for distributions that are located near the interface 2,3 (i.e., for z_0 and $\Delta z \ll 1/Q_2''$). Here, we apply a first-order Taylor series expansion to the exponential term in the expression for $Y_0(Q_2)$, yielding

$$Y_0(Q_2) \cong \int_{z=0}^{t_2}\rho(z)[1+Q_2''z]dz = \rho^{2D} + Q_2''z_0\rho^{2D}, \tag{13}$$

where $z_0=\int_{z=0}^{t_2}\frac{\rho(z)zdz}{\rho^{2D}}$ is the average height of the distribution. The term $Y_0(-Q_2)$ is also expanded similarly, to obtain

$$\frac{Y(Q_2)}{\rho^{2D}} \cong |E_2(Q_2)|^2\{1 + R_2(Q_2) + 2\sqrt{R_2(Q_2)}A(Q_2)\cos[v_2(Q_2) - 2\pi P(Q_2)] + z_0Q_2''[1 - R_2(Q_2)]\}. \tag{14}$$

We now evaluate the first-order term in the expansion of the attenuation factor, $\exp(+Q_2''z)$, used in the above derivation, for the case of an elemental distribution in an aqueous medium (the attenuation length of 17 keV x-rays in water is $\sim$10 mm). At the critical angle of the aqueous medium (Q

$=0.022$ Å^{-1}), the contribution of this term to the fluorescence yield is less than one percent for distribution widths less than ~1200 Å and becomes smaller with increasing angles (since it is inversely related to Q). Since the Ti distribution probed in this study is only ~10–20 Å thick, it is reasonable to exclude this attenuation term. In this case, the expression for fluorescence yield becomes

$$\frac{Y(Q_2)}{\rho^{2D}} \cong |E_2(Q_2)|^2[1 + R_2(Q_2) + 2\sqrt{R_2(Q_2)}A(Q_2)\cos\{v_2(Q_2) - 2\pi P(Q_2)\}]. \quad (15)$$

In an XSW experiment Y is measured while R and v are known (in principle) from a prior analysis of the x-ray reflectivity data. The only unknowns therefore are $A(Q_2)$ and $P(Q_2)$, which can be extracted from the data using the model-independent method discussed below. This equation is similar to that used in Bragg-XSW analysis where, however, A and P are treated as constants for each Bragg diffraction condition. In long-period XSW measurements, A and P are continuous functions of Q_2 corresponding to the continuous measurement of fluorescence yield vs Q_2 data. Here, we adopt an approach similar to the Bragg-XSW analysis for the TER-XSW data by creating artificial segments in the data and obtaining the model-independent information for each segment.

Applying a first-order Taylor series expansion to A and P over a region of width ΔQ_2 centered at $Q_2=Q_2^0$, we obtain: $A(Q_2)=A_{Q_2=Q_2^0}+(\frac{dA}{dQ_2})_{Q_2=Q_2^0}(Q_2-Q_2^0)$ and $P(Q_2)=P_{Q_2=Q_2^0}+(\frac{dP}{dQ_2})_{Q_2=Q_2^0}(Q_2-Q_2^0)$, and substituting in Eq. (15)

$$\frac{Y(Q_2)}{\rho^{2D}} = |E_2(Q_2)|^2\left[1 + R_2(Q_2) + 2\sqrt{R_2(Q_2)}\left\{A_0 + \frac{dA_0}{dQ_2}(Q_2 - Q_2^0)\right\}\cos\left\{v_2 - 2\pi\left(P_0 + \frac{dP_0}{dQ_2}\right)(Q_2 - Q_2^0)\right\}\right]. \quad (16)$$

Expanding the expression to first order in the gradient terms, the above equation transforms to

$$\frac{Y}{\rho^{2D}} = |E_2(Q_2)|^2\left[1 + R_2 + 2\sqrt{R_2}A_0\cos(v_2 - 2\pi P_0) + 2\sqrt{R_2}\left\{\frac{dA_0}{dQ_2}\cos(v_2 - 2\pi P_0) + A_0 2\pi\frac{dP_0}{dQ_2}\sin(v_2 - 2\pi P_0)\right\}(Q_2 - Q_2^0)\right]. \quad (17)$$

This shows that the fluorescence yield near Q^0 is determined by A_0 and P_0 while the variation farther away from Q^0 is controlled increasingly by the gradient terms $(\frac{dA}{dQ_2})_{Q_2=Q_2^0}$ and $(\frac{dP}{dQ_2})_{Q_2=Q_2^0}$. The four unknowns in the above equation (A_0, P_0, $\frac{dA_0}{dQ_2}$, and $\frac{dP_0}{dQ_2}$) are model-independent parameters that can be extracted by a fit of Eq. (17) to the measured yield data vs. Q_2 in a region of width ΔQ_2. If the entire range of data is divided into separate segments of width ΔQ_2, and each segment is fit separately to the above equation, a series of amplitudes and phases (and their gradients, if needed) can be obtained. If the chosen segment width ΔQ_2 is sufficiently small, such that there is no significant variation in the structure factor for the elemental distribution over this region, the fluorescent yield variation within each segment can be fit with just the A_0 and P_0 of that segment. The elemental distribution $\rho(z)$, which is the inverse Fourier transform of the elemental-specific structure factor, $F(Q_2)=A(Q_2)\exp[i2\pi P(Q_2)]$, can then be directly generated by the Fourier inversion, using the relation

$$\rho(z) = \frac{1}{2\pi}\int_{-\infty}^{+\infty} A(Q_2)\exp\{i2\pi P(Q_2)\}\exp(-iQ_2z)dQ_2 \approx \frac{1}{2\pi}\sum_j A_j\exp(i2\pi P_j)\exp(-iQ_2^jz)\Delta Q_2. \quad (18)$$

Here, the continuous Fourier transformation integral has been approximated to a finite summation and this summation is over all segments into which the data is divided, with Q_2^j being the center of the jth segment, and ΔQ_2 the width of each segment. The recovered profile will be intrinsic with sufficient sampling of A and P (i.e., in terms of the sampling frequency which determines the size of the Fourier window and the maximum momentum transfer which determines the spatial resolution of the recovered profile).

Equation (17) is also applicable to the case where the x-ray attenuation over the extent of the elemental distribution is considerable (e.g., for a 1000 Å or wider distribution in an aqueous medium), if the extra term $z_0Q_2''[1-R_2(Q_2)]$ is added in the expression for the fluorescence yield [Eq. (14)]. Similarly, for the limiting case of a narrow distribution [Eq. (12)], the z_0-dependent attenuation terms can be included in the analysis. In these cases however, there is the additional unknown quantity, z_0, which can be used as an extra parameter during the model-independent fit of the data. This also allows for a consistency check since the average height of the elemental profile is also determined from the recovered profile, i.e., from $P(Q_2)$.

III. EXPERIMENTAL

Measurements were conducted on a trilayer system consisting of TiO_2, Si, and Mo layers grown on Si substrate. The starting substrate was a 2.5-mm-thick, single-side polished, 150-mm-diameter Si(001) wafer. The wafer surface had a root mean-square (rms) roughness of 3 Å as measured using x-ray reflectivity. The wafer was diced into several 12-mm by 37-mm sized samples. These rectangular Si substrates were then mounted on a specially designed plate to hold the individual pieces and were coated using sputter deposition with Si and Mo layers (with expected thicknesses of 540 and 60 Å, respectively). The top layer of TiO_2 was then grown using atomic layer deposition (ALD) (Ref. 32) and was expected to be 10-Å thick. The samples were degreased with acetone, methanol, and deionized water in a sonicator before the sputter deposition, ALD growth, and x-ray measurements.

Ex situ x-ray measurements were performed with the sample held in air. The *in situ* x-ray measurements were

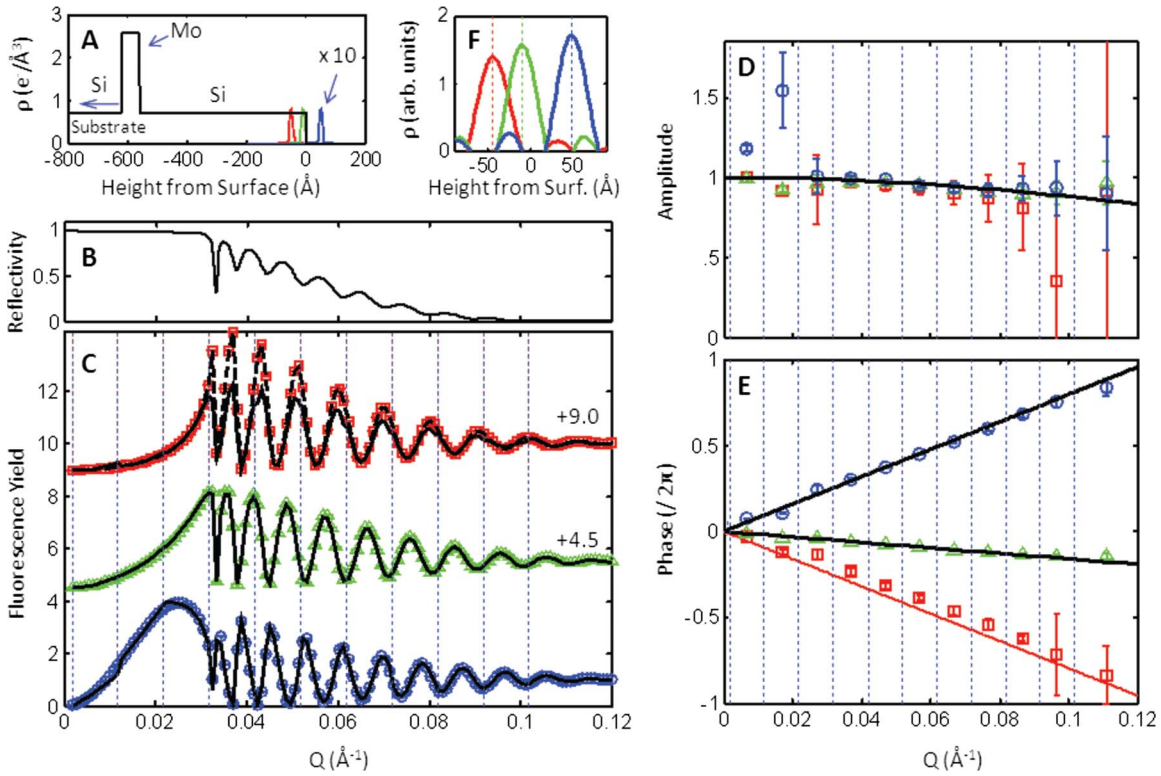

FIG. 2. (Color online) Model-independent formalism applied to simulated fluorescence yield data for Si/Mo bilayer (with thicknesses of 560 and 60 Å) on Si substrate, for three assumed Gaussian elemental distributions, each with σ=5 Å. (A) The density profile of the bilayer system (black) used to calculate the reflectivity and phase of reflected wave (R and ν). The three elemental distributions shown are for Gaussian profiles centered at 50 Å above (blue), 10 Å below (green), and 50 Å below (red) the top Si surface. (B) Simulated reflectivity vs Q calculation for the Si/Mo bilayer at incident x-ray energy of 17 keV. (C) The simulated fluorescence yield data (symbols) and the model-independent fits (solid lines, based on electric field intensities in vacuum). The dashed black line shown for the case of the Gaussian located 50 Å below the surface is the model-independent fit based on the use of electric field intensities inside the Si layer and including x-ray absorption in the medium as described by Eq. (12). The data are offset vertically for clarity. [(D) and (E)] The model-independently derived amplitudes and phases (symbols) as well as the A and P expected based on the assumed models (lines). (F) The reconstructed density profiles from Fourier-inversion of the derived A and P.

conducted in a thin-film cell geometry[21,33] with a 7-μm Kapton film used to enclose the aqueous layer ($\sim$2 μm) on the sample surface. The aqueous solution used for the *in situ* measurement was a 0.2-mM RbOH solution at pH 10.3. This solution condition was chosen as part of an effort to measure ion distributions at the oxide-water interface, the results of which will be published elsewhere.

X-ray reflectivity and x-ray standing waves measurements were conducted at beamline 33BM-C at the Advanced Photon Source (APS) at Argonne National Laboratory. The incident x-ray energy during the measurements was 17.00 keV. The measured x-ray beam size at the sample was 0.05-mm high by 1-mm wide, with a flux of $\sim 2\times 10^{10}$ photons/s. The reflected intensity was measured using a Cyberstar scintillation detector while the Ti $K\alpha$ fluorescence was collected using a SII NanoTechnology Inc. Vortex detector. An ion chamber with N_2 gas was used to monitor the incident flux to which the data was normalized before analysis. The Ti-XSW data were obtained by subtracting a linear background around the Ti $K\alpha$ yield peak in the multichannel analyzer XRF spectra. Corrections due to the XRF detector dead time[34,35] and due to the variation in the beam footprint on the sample with incident angle were applied to the yield data. Data for $Q<0.026$ Å^{-1}, where beam footprint on the sample exceeded the sample length, were not included in the reflectivity and Ti-yield analysis.

The Ti coverage was estimated from x-ray fluorescence yield measured in both *ex situ* and *in situ* environments. Calibration of the absolute elemental coverage used the Sr $K\alpha$ yield from a standard sample (a Sr-implanted Si wafer with a deposition density of 10.6 Sr/nm^2, calibrated with Rutherford backscattering[35]), taking into account the differences in the elemental absorption cross section and the $K\alpha$-fluorescence cross section (yield) for the two elements, as well as the difference in the detector efficiency at the two fluorescence energies. The measured fluorescence yields were corrected for attenuation through air before reaching the detector while additional corrections for attenuation of the fluorescence yield as well as of the incident beam through the Kapton and solution layers were included for the *in situ* measurements.

IV. RESULTS

A. Results from simulations

We first demonstrate the feasibility of the model-independent formalism by applying it to simulated fluores-

cence yield data generated from a model calculation for incident x-ray energy of 17.00 keV. The simulated data was generated by an augmentation of Parratt's recursion formulation.[36–38] The model structure is a Si/Mo bi-layer on a Si substrate [black line in Fig. 2(A)], where the Si and Mo layers are 560 and 60-Å thick, respectively, that is similar to the samples investigated below in the experimental studies. The simulated reflectivity from this layered structure with $\sigma=1$ Å rms interface roughnesses is shown in Fig. 2(B). Notice that there is a sharp drop in the reflectivity at the Si critical angle corresponding to $Q_C=0.032$ Å^{-1}. The target elemental profiles that will be recovered are represented by Gaussian distributions [shown in Fig. 2(A)] with widths of $\sigma=5$ Å, centered at 50 Å above, 10 Å below, and 50 Å below the top Si surface. (In these simulations the target elemental profiles will not affect the primary E fields by refraction or absorption). These height differences lead to differences in the simulated fluorescence yield data for the three cases [Fig. 2(C)], where the first peak in the TR region is present below the Si critical angle ($Q_C \sim 0.032$ Å^{-1}) for the Gaussian located above the surface while almost at and slightly above Q_C for the profiles centered 10 and 50 Å below the surface, respectively. This is consistent with a XSW node being at the top surface at $Q=0$ and the first XSW antinode sweeping inward toward the surface as the incident angle increases and arriving at the top Si surface when the incident angle equals Q_C for Si.

The simulated yield data is fitted with the model-independent formalism discussed above to recover the elemental profiles, first using the electric fields in vacuum (i.e., using R_1, v_1, and E_1 corresponding to the air-Si interface). This is done to illustrate the situation in which the elemental profile is initially unknown. The simulated XRF yield data are assigned a fixed uncertainty of 0.1%. The data are divided into segments of width $\Delta Q=0.01$ Å^{-1} (which gives sufficient sampling to locate distributions up to $2\pi/\Delta Q=600$ Å above the surface) as shown by the vertical dashed lines in Fig. 2(C) and the fluorescence yield within each segment is fitted with only two parameters corresponding to the amplitude and phase [$A(Q^j)$ and $P(Q^j)$]. Note that the calculated fluorescence yield does not show any significant discontinuities at each segment boundary, suggesting that the chosen segment width was appropriate. The model-independently derived A and P [symbols in Figs. 2(D) and 2(E)], are compared with the expected values of A_{calc}, and P_{calc}, [lines in Figs. 2(D) and 2(E), respectively] that were obtained from the calculated structure factors, F, for the Gaussian profiles, given by

$$F(Q) = \exp\left(-\frac{1}{2}\sigma^2 Q^2\right)\exp(iQZ_0)$$
$$= A_{calc}(Q)\exp\{i2\pi P_{calc}(Q)\}, \quad (19)$$

where z_0 is the center and σ the width of the Gaussian layer. Using Eq. (18), the Fourier inversion of the derived amplitudes and phases yields the density profiles [Fig. 2(F)]. The recovered mean positions of the distributions in Fig. 2(F) match (within 0.5 Å) the expected z_0 values from the original Gaussians shown in Fig. 2(A) for the cases of 10 Å below the surface and 50 Å above the surface. In these cases, the fluorescence yield data is also reproduced well by the formalism [solid lines in Fig. 2(C)]. The recovered position for the Gaussian located 50 Å below the surface, however, differs from the actual position by 6 Å. In that case, the fluorescence yield data are not well reproduced by the model-independent formalism [red line in Fig. 2(C)]. This is due to the use of electric field intensities appropriate for the vacuum layer instead of those present in the silicon substrate (although this limitation was also present for the profile that was 10 Å below the surface; in that case, the change in electric field intensities was small due to its proximity to the interface).

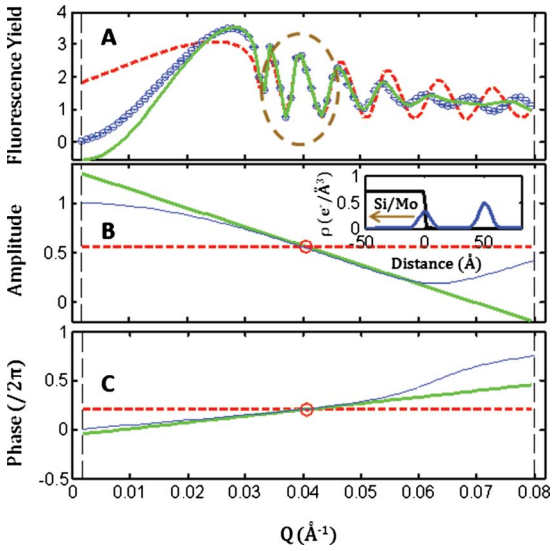

FIG. 3. (Color online) Illustration of the relative benefits of the model-independent analysis using fixed values of $A(Q^0)$ and $P(Q^0)$ within segment ΔQ at Q^0, versus the use of linear gradient terms to describe the variation in A and P within each segment. Data are simulated for a Si/Mo bilayer on Si substrate for a two-layer distribution of the element of interest consisting of Gaussians centered at and 50 Å above the surface (shown in inset in 3B), each with $\sigma=5$ Å. (A) The simulated fluorescence yield data (blue circles), and two model-independent calculations: without (dashed red line) and with (solid green line) the gradient terms of A and P included. In the first case, the yield is calculated for the range shown ($0<Q<0.08$ Å^{-1}) using $A=A(Q^0)$ and $P=P(Q^0)$. In the second case, additional slope parameters dA/dQ and dP/dQ are included based on the gradients of A and P obtained from the actual elemental structure factor at Q^0. [(B) and (C)] The variation in A and P, respectively, for the actual elemental distribution (blue circles), along with the model-independent calculation with fixed values defined at $Q^0=0.04$ Å^{-1} (red dashed lines), and when the gradient terms are included (green lines).

We then used the electric field intensities inside the Si layer to fit the fluorescence yield for the Gaussian located 50 Å below the surface. This was done by using the reflection coefficients (i.e., R_2, v_2, and E_2) corresponding to the Si-Mo interface in the analysis. In this case, we used the phase gradient parameter dP/dQ_{Si} during the fit, in addition to the A and P parameters since the distribution was at a large height with respect to the Si-Mo interface (since the Gaussian located 50 Å below the surface is at a height of

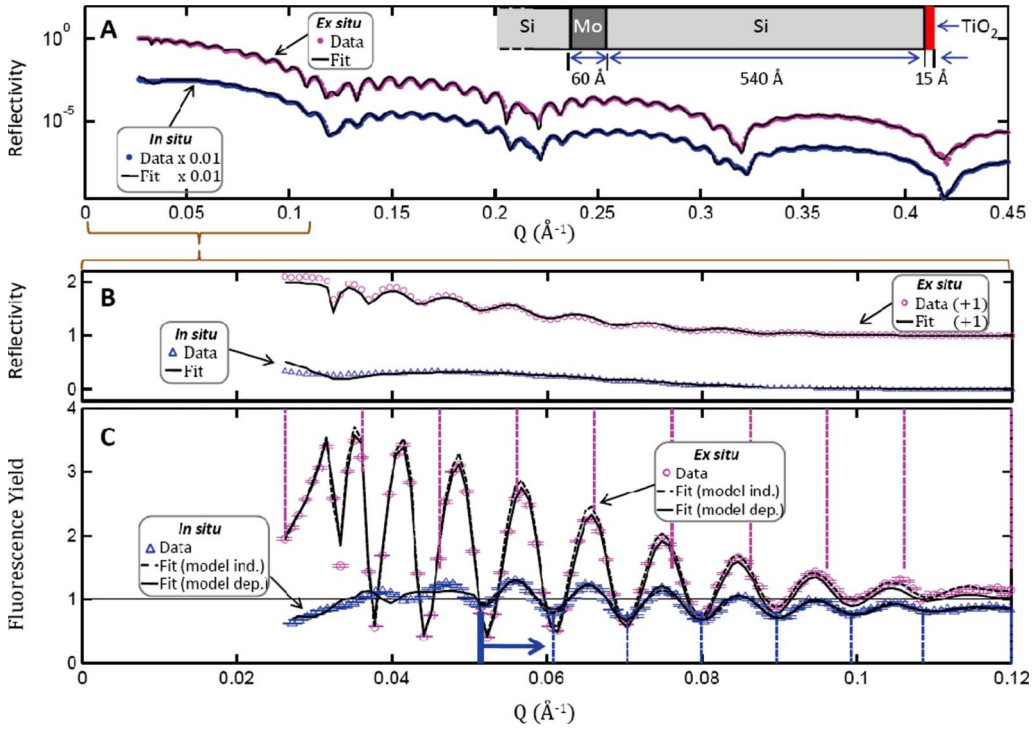

FIG. 4. (Color online) Model-independent analysis of measured *ex situ* and *in situ* reflectivity and Ti yield for the TiO_2-Si-Mo-Si substrate system. (A) The reflectivity data (dots) in absolute units measured in air (magenta) and in contact with aqueous solution (blue). The model fits are shown as lines. Error bars are not shown for clarity. Typical statistical uncertainty in the reflectivity data was ~0.5% while a minimum uncertainty of 2% based on systematic errors was assigned to the data before analysis. The *in situ* reflectivity data (blue symbols) is multiplied by 0.01. (B) A highlight of the reflectivity data in the $Q<0.12$ Å^{-1} range corresponding to the full Ti-fluorescence yield data (circles, panel C). The parameters derived from the reflectivity analysis were based on the fit of the full-range (shown in A). (C) The Ti-yield data (circles) measured in air (magenta) and in contact with an aqueous solution (blue). The vertical dashed lines show the segments into which the data were divided for the model-independent analysis (a constant segment width of $\Delta Q=0.01$ Å^{-1} was used). Model-independent fits (dashed lines) and model-based fits (solid lines) are shown. The blue arrow shows the range of *in situ* data included in the fit ($Q>0.05$ Å^{-1}). Inset in A shows the schematic of the trilayer sample in air.

510 Å from the Si-Mo interface) and therefore the phase variation could not be treated as constant over the segment width ($\Delta Q_{Si}=0.01$ Å^{-1}). In this case it was also important to include x-ray absorption inside the Si layer, which was significant below the critical angle. This was done by use of Eq. (12) and using z_0 as an additional parameter in the fit. This approach gave excellent agreement with the fluorescence yield data, both above and below the critical angle [dashed line in Fig. 2(C)]. The average height of the distribution was obtained simply from the parameter z_0 [Eq. (12)], which was found to be 509.9 Å with respect to the Si-Mo interface, or 50.1 Å below the top surface (close to the expected 50 Å). The height of the distribution was also obtained from the density profile reconstructed from the derived amplitudes and phases, which was found to be centered at 510 Å above the Si-Mo interface, exactly as expected and consistent with the derived value for z_0. In the calculations described above for the Gaussian distributions, the model-independent calculations used the E fields based on the Si/Mo bi-layer, and neglected any contribution to the electric field intensity due to the presence of the elemental profile. When the presence of the elemental distribution significantly alters the E fields, it should be included in the E-field calculations. Since the reflectivity of the system is measured in an XSW experiment along with the fluorescence yield, this is automatically included when the E fields are based on the analysis of the experimental reflectivity data.

The analysis so far has extracted $A(Q)$ and $P(Q)$ of the elemental profile using $\Delta Q=0.01$ Å^{-1}, and the gradient parameters were neglected (except for the last example in which the reflection coefficients were referenced to the Si-Mo interface and where the phase-gradient term was included). We now illustrate the conditions under which fixed amplitudes and phases can be used and when the gradient parameters become important. This is shown in Fig. 3 for a distribution consisting of two Gaussian layers located at and 50 Å above the surface [inset in Fig. 3(B)]. The simulated fluorescence yield data [blue circles in Fig. 3(A)] is compared against two model-independent calculations. The first calculation [dashed red line in Fig. 3(A)] assumes $A(Q)=A(Q^0)$ and $P(Q)=P(Q^0)$, with $Q^0=0.04$ Å^{-1} chosen to be at the center of the calculation range ($\Delta Q=0.08$ Å^{-1}). Note that this calculation agrees well with the simulated data near $Q=Q^0$ extending over a Q range where the assumed values of $A(Q^0)$ and $P(Q^0)$ [red dashed lines in Figs. 3(B) and 3(C)] approximate the actual variation in $A(Q)$ and $P(Q)$ [thin blue lines in Figs. 3(B) and 3(C)]. This range of $Q=0.035-0.045$ Å^{-1} is highlighted in Fig. 3(A). However,

this calculation deviates significantly from the simulated data as Q deviates significantly from Q^0. The second calculation [green line in Fig. 3(A)] shows that inclusion of the terms that describe the gradient of A and P within ΔQ [i.e., $dA/dQ(Q^0)$ and $dP/dQ(Q^0)$] substantially increases the range over which the model-independent calculation agrees with the simulated data, again because this provides a better approximation for the actual variation in A and P within the segment width [blue line, Figs. 3(B) and 3(C)]. From this example, it becomes evident that the choice of approach in analyzing the fluorescent yield data (i.e., using fixed amplitudes and phases for each segment or including linear gradient terms) will depend on the specific shape of the element-specific distribution and the choice of the segment widths. Consequently, some prior knowledge of the potential physical range of the elemental distribution is helpful in choosing the segment width. The appropriateness of the chosen segment width can be directly evaluated by the ability to reproduce the observed fluorescence yield data.

B. *Ex situ* experimental results

The x-ray reflectivity measurements for the $TiO_2/Si/Mo$ on Si-substrate system are shown in Fig. 4(A) (magenta dots). We begin with a qualitative assessment of the data. Two distinct periods of oscillations are visible in the data. The longer oscillation period ($\Delta Q \sim 0.1$ Å^{-1}) arises from interference between x-rays reflected from the Si-Mo and Mo-Si interfaces suggesting a Mo layer thickness of $2\pi/\Delta Q \sim 60$ Å. The fine period oscillations have a approximately nine times finer Q spacing corresponding to the Si layer thickness of ~540 Å. It can be seen that the fine period oscillations in the data are weaker for $Q < 0.12$ Å^{-1} and become strong at larger Q. This is because of the increased attenuation of x-rays passing through the top Si layer to reach the Si-Mo interface at low angles, thereby causing reduction in the interference fringes. There is also a gradual reduction in the strength of these finer-scale oscillations with increasing Q. This reduction is associated with interfacial roughness, of the interface above or below the Si layer. The observation of significant oscillations from the Mo thickness that are still pronounced at high Q suggests that the Si-Mo and Mo-Si interfaces have sharper widths than the $Si/TiO_2/Air$ interfaces.

A quantitative analysis of these data is necessary to obtain the total electron-density profile which is needed to calculate the electric field intensities. These electric field intensities are used in the analysis of XSW fluorescence yield data to obtain the precise element-specific profile of the fluorescing species. The x-ray reflectivity analysis was performed using least-squares fitting by comparing the data to model calculations based on Parratt's recursion formalism.[30,31] Interfacial roughness was incorporated as a Debye-Waller factor multiplied by the Fresnel coefficients for each interface.[30] The system was modeled as separate TiO_2, Si, and Mo layers on a semi-infinite Si substrate. It is important to note that x-ray reflectivity is sensitive primarily to the total electron density and therefore the chemical composition of the different layers has only a minimal influence on these data. Here, our prior knowledge of the multilayer structure was used to guide our initial choices of the refractive index parameters ($n = 1 - \delta - i\beta$) for the three materials that were initially based on their respective bulk values. Two parameters were used to describe the jth layer, a thickness (t_j), and a density factor (X_j) to allow for changes in the layer density with respect to the assumed bulk density of the material [shown by dashed horizontal lines in Fig. 5(A)]. The refractive index used for jth layer was $n_j = n_j^{Bulk} X_j$. Interfacial roughness for the interface between the j and $j+1$ layers was included as the parameter σ_j. The calculation [Fig. 4(A), black line as indicated for *ex situ* case] reproduces all of the qualitative features present in the data and has an R factor of 0.1 (defined in Table I). The structural parameters determined from the fit are shown in Table I (sample 1). The Si and Mo layer thicknesses determined from the analysis are close to the values that we estimated from qualitative assessment and the interfaces above the Si layer are indeed rougher than the ones below it. The thickness of the top TiO_2 layer is determined to be 16.7 ± 0.1 Å. The complete density profile based on this model analysis [black lines in Fig. 5(A)] was used to calculate the electric field intensities required to analyze the XSW data.

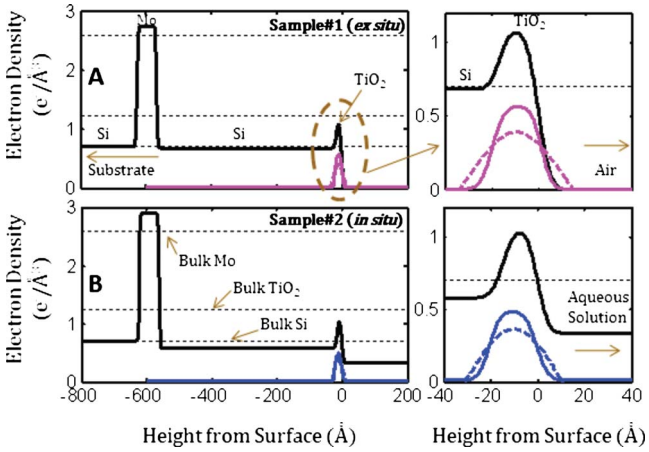

FIG. 5. (Color online) The density profiles for the TiO_2-Si-Mo-Si substrate system based on analysis of reflectivity measurements (black lines) for (A) the *ex situ* analysis and (B) the *in situ* analysis. The horizontal black dotted lines show the expected bulk electron density of each material. These interfacial profiles include the interfacial roughness obtained by the reflectivity analysis (see Table I). The TiO_2 profiles based on the analysis of Ti-yield data are also shown for model-independent (dashed) and model-based (solid) cases, these profiles are scaled to absolute units based on the Ti coverage measured from XRF.

The Ti $K\alpha$ fluorescence yield data measured in air is shown in Fig. 4(C) (magenta circles). The first peak in the fluorescence yield data occurs at $Q \sim 0.032$ Å^{-1}, the critical angle of the system [Fig. 4(B)], which reveals that the Ti distribution is located at the surface, as expected. The yield modulations at increasing Q [Fig. 4(C)] arise from the oscillations in reflectivity due to the Si layer thickness [Fig. 4(B)].

For the model-independent analysis, the data was divided into segments of width $\Delta Q = 0.01$ Å^{-1} [outlined in Fig. 4(C) by dashed vertical magenta lines] and fit using the model-

TABLE I. Parameters derived from the fit of the reflectivity data measured in air and under an aqueous solution.

	Ex situ results (sample 1)	*In situ* results (sample 2)
Fit quality[a]		
R factor	0.10	0.08
χ^2	55	37
Structure[b]		
t_{TiO_2} (Å)	16.7 ± 0.1	14.9 ± 0.2
t_{Si} (Å)	549.3 ± 0.2	546.2 ± 0.3
t_{Mo} (Å)	60.67 ± 0.02	60.65 ± 0.01
X_{TiO_2} [c]	0.88 ± 0.01	0.86 ± 0.01
X_{Si}	0.97 ± 0.01	0.83 ± 0.02
X_{Mo}	1.06 ± 0.01	1.12 ± 0.01
$\sigma_{Air\text{-}TiO_2}$ (Å)	5.73 ± 0.08	5.0 ± 0.1
$\sigma_{TiO_2\text{-}Si}$ (Å)	4.9 ± 0.1	5.4 ± 0.2
$\sigma_{Si\text{-}Mo}$ (Å)	3.54 ± 0.02	3.40 ± 0.02
$\sigma_{Mo\text{-}Si}$ (Å)	3.75 ± 0.02	3.51 ± 0.02
Extrinsic		
t_{H_2O} (μ)	0	1.39 ± 0.04
t_{Kap} (μ)	0	7.5 ± 0.1
X_{H_2O}	N/A	1[d]
X_{Kap}	N/A	1[d]
Angle avg., δQ_{Ref}(Å^{-1})	0	0.048 ± 0.001 [e]

[a]Least-squares fit was guided by Chi-squared deviation of the data from the calculation, defined as $\chi^2 = 1/n\Sigma(y\text{-}f)^2/\varepsilon^2$, where y denotes the data, f the calculation, ε the uncertainty in the data, and n the number of data points. Quality of fit is also indicated by parameter R representing the average deviation of data points from calculation, or $R = 1/n\Sigma|(y\text{-}f)/y|$, where $\|$ denotes the absolute value.

[b]Uncertainties are based on a minimum 2 percent error-bar enforced on the data points when the statistical uncertainty was smaller.

[c]X denotes the fraction of the electron density of the layer with respect to the electron density of bulk material.

[d]Parameter fixed during the fit.

[e]A bending radius of curvature of 31 m can be estimated based on δQ_{Ref} for a vertical x-ray beam size of 50 μ.

independent formalism described above. Here the reflectivity and the phase of the reflectivity coefficient are based on Parratt's formulation applied to the electron-density model displayed in Fig. 5(A). Note that this model includes an initial rough estimate (from reflectivity analysis) for the presence of the TiO_2 layer and thus R_1 and v_1 correspond to the air-TiO_2 interface. As seen in Fig. 4(C), the model-independent fit (dashed black line as indicated for the *ex situ* case) is in very good agreement with the data, giving an R factor of 0.03 (Table II). The amplitudes and phases ($\underline{A}$ and P) derived from each segment are shown in Fig. 6 (magenta circles); these A and P values reveal direct information about the 1D Ti atomic-density profile. The negative slope in phase variation indicates that the Ti distribution is centered *below* the surface, which is expected since the origin was chosen to be the air-TiO_2 interface. The Q variation in the derived amplitudes and phases in the Q range of analysis is consistent with a single layer of Ti, as expected. The extrapolation of $A(Q)$ in the limit of $Q \rightarrow 0$ (i.e., $A_{Q=0}$) gives the value $A_{Q=0}=0.86$ (or 86% of the total coverage). This $Q=0$ value of element-specific amplitude is expected to be equal to unity for any elemental distribution. That $A_{Q=0}$ is less than unity indicates the presence of an incoherent contribution to the fluorescence yield. We will provide explanations for possible sources of this incoherency in the discussion section.

The Fourier-inversion described by Eq. (18) is then used on the set of A_j and P_j values shown in Fig. 6 to generate the Ti profile centered at 9.3 Å below the surface as shown in Fig. 5(A). This Ti profile is converted to absolute units of $e/\text{Å}^3$ for a TiO_2 layer [Fig. 5(A), dashed magenta line], based on the measured Ti-number density from XRF (Table II) and the electron density of TiO_2 (assuming all Ti are in the form of TiO_2). This conversion is done so there can be a direct comparison of the XSW-derived profile to the adjoining electron-density profile that was derived from the reflectivity analysis.

TABLE II. Parameters derived from model-independent and model-based analyses of the Ti $K\alpha$ x-ray standing wave data measured in air and under an aqueous solution. Ti coverage estimate based on x-ray fluorescence measurements is also reported.

	Ex situ results (sample 1)	*In situ* results (sample 2)
Model independent		
Fit quality		
R factor	0.03	0.02
χ^2	19	1.9
Structure[a]		
z_0 (Å)	−9.3	−10.0
Δ (Å)	~30	~30
Extrinsic		
$A_{Q=0}$	0.86	0.60
Angle avg., $\delta Q_{\mathrm{Ref}}(\mathrm{Å}^{-1})$	0	0.037 ± 0.001 [b]
$t_{\mathrm{H_2O}\ equivalent}$ (μ) [c]	0	10.8 ± 0.6
Model dependent		
Fit quality		
R factor	0.05	0.02
χ^2	31	3
Structure		
z_0 (Å)	-9.2 ± 0.3	-10.5 ± 1
Δ (Å)	21 ± 3	20 ± 3
Extrinsic		
$A_{Q=0}$	0.86[d]	0.60[d]
Angle avg., $\delta Q_{\mathrm{Ref}}(\mathrm{Å}^{-1})$	0	0.037 ± 0.001 [b]
$t_{\mathrm{H_2O}}$ (μ)	0	3.8 ± 0.6
$t_{\mathrm{K}ap}$ (μ)	0	8.3 ± 0.7
X-ray fluorescence		
Θ_T (Ti atoms/Å^2)	0.31[e]	0.25[e]

[a]The model-independent structural parameters shown were derived from the fit parameters A and P used in the fit.

[b]A bending radius of curvature of 40 m can be estimated based on δQ_{Ref} for a vertical x-ray beam size of 50 μ.

[c]This is used to calculate $|E_2(Q_2)|^2$ at the water-TiO_2 interface needed for the model-independent analysis (accounts for attenuation of the incident x-ray beam through Kapton and solution layers).

[d]Value fixed based on the information from model-independent results.

[e]This is an estimate based on the procedure described in the experimental section. The uncertainties in this parameter were systematic and arose from the nominal attenuation corrections of the Ti $K\alpha$ fluorescence yield through air, Kapton, and solution layers (for the *in situ* data) that were based on the detector geometry as well as corrections for the detector efficiency.

A model-based analysis was done to confirm the model-independent results; this was based on exact calculation of E fields throughout the extent of the total structure and use of Eq. (8) to calculate the fluorescence yield from the model Ti structure. The model used was a rectangular profile with rounded edges, represented by the product of two error functions. The interfacial widths were fixed at the values derived from the reflectivity analysis for the air-TiO_2 and TiO_2-Si interfaces. Other parameters used during the fit were a scale factor, and the thickness and position of the Ti layer. This model-dependent fit led to an R factor of 0.05 [solid black line in Fig. 4(C), Table II]. An incoherent fraction of 0.14 (i.e., $1-A_{Q=0}$) was assumed in the analysis based on the information from the model-independent analysis (Table II). This parameter was fixed since it covaries with the width of the Ti layer. This incoherent component was modeled as a relatively broad Gaussian layer centered at the surface. We used a width of 200 Å, which was sufficiently broad to make the structure factor for this layer insignificant over the Q range of data studied. The amplitudes and phases of the Ti distribution including the incoherent component are plotted in Fig. 6 (magenta lines), indicating very good agreement with the model-independent results. The model-based density profile (Fig. 5, solid magenta line) shows that the Ti

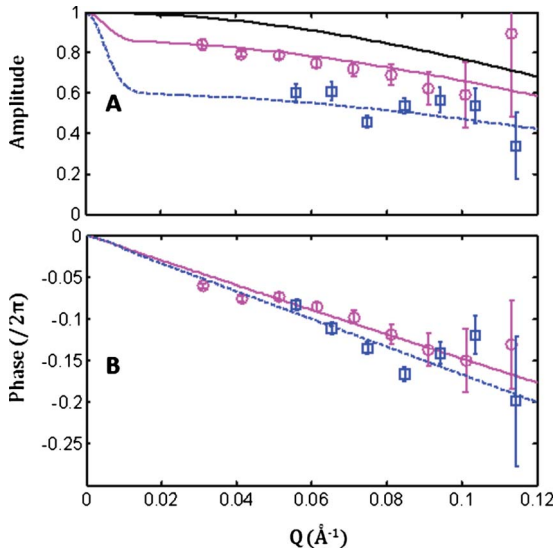

FIG. 6. (Color online) (A) Amplitudes and (B) phases (symbols) extracted from the model-independent analysis for the sample measured in air (magenta) and in contact with an aqueous solution (blue). The A and P variation based on the model analysis are shown in lines. Note the difference in the extrapolated value of $A_{Q=0}$ for the *ex situ* and *in situ* results. Also shown are the A vs Q variation (black line) for the *ex situ* case if the distribution were fully coherent (i.e., with $A_{Q=0}=1$).

distribution is centered at 9.2 ± 0.3 Å below the surface, which agrees with the results derived from the model-independent analysis. This is also a good agreement with the value expected based on reflectivity, which is 8.4 Å (i.e., half of the TiO_2 layer thickness found from the reflectivity analysis), especially since reflectivity is not an element specific technique. The Ti-layer thickness of 21 ± 3 Å obtained from the model analysis of the XSW data can be compared against that derived from two other independent methods, namely, reflectivity and x-ray fluorescence. The reflectivity measurements reveal a TiO_2 thickness of 16.7 ± 0.1 Å. The differences are not unexpected given the poorer spatial resolution of the XSW data. Based on a $Q_{max}-Q_{min}$ defined resolution, the XSW data had a resolution of ~33 Å while the reflectivity had a 7 Å resolution. The estimate of the TiO_2 film thickness based on XRF yield is 10 Å. This value is based on the coverage of 0.31 Ti/Å^2 estimated from the measured Ti $K\alpha$ counts (at $Q=0.15$ Å^{-1}) using the procedure described in the experimental section and assuming bulk density of TiO_2 to calculate the TiO_2 thickness from the coverage.

C. *In-situ* experimental results

The *in situ* reflectivity data [Fig. 4(A)] were measured on a second sample that was nominally similar to that used for the *ex situ* measurements. The data are similar in terms of the period of oscillations suggesting similar structural parameters. The *in situ* data are characterized by a substantially diminished magnitude of oscillations in the reflectivity signal compared to the *ex situ* data, particularly in the low-Q region [Fig. 4(B)]. This is due to both intrinsic and extrinsic factors. There is a reduced density contrast at the water-TiO_2 interface which reduces the visibility of these fringes. We also find that there is a bending of the sample due to stress on the sample edges from tension in the Kapton film which was used to confine the aqueous solution at the sample surface.[33] This bending of the crystal further reduces the visibility of the reflectivity fringes due to "angular averaging" because the incident beam effectively has a finite range of incident angles along the length of the beam footprint on the sample.

The model used to fit the *in situ* reflectivity data [black line in Fig. 5(B)] was similar to that used in the *ex situ* analysis, except additional layers of water and Kapton were included. Layer thicknesses, density factors, as well as the interfacial roughnesses were allowed to vary during the fit. An additional parameter δQ_{Ref} was used to include the effect of angular averaging, based on the treatment described by Libera,[33] where the angular range over which the data are averaged at any Q is described by $\delta Q(Q)=\frac{Q_{\mathrm{Ref}}}{Q}\delta Q_{\mathrm{Ref}}$, where δQ_{Ref} is the angular averaging magnitude at a reference Q, here, $Q_{\mathrm{Ref}}=0.01$ Å^{-1}. The parameters obtained from the *in situ* analysis are listed in Table I (sample 2). The good agreement in the structural parameters for the two separately prepared samples measured under different conditions shows the reproducibility of our sample preparation conditions.

Comparison of the *in situ* Ti-yield data [Fig. 4(C)] with the *ex situ* data shows that the observed oscillation period is very similar for $Q>0.07$ Å^{-1} but differs significantly for $Q<0.05$ Å^{-1}. This is due to the angular averaging described above, which is most significant at lower incident angles [Figs. 4(B) and 4(C)]. As for the reflectivity data [Fig. 4(B)], the magnitude of the fluorescence yield oscillations [Fig. 4(C)] is considerably smaller for the *in situ* data.

The *in situ* Ti-yield analysis was restricted to $Q>0.05$ Å^{-1} [as indicated by the blue arrow, Fig. 4(C)]. Data outside of this range was not used for analysis because the calculations could not explain the measured fluorescence yield oscillations below $Q=0.05$ Å^{-1}, as seen from the disagreement in the plot [Fig. 4(C)]. This is because the angular averaging (δQ) at these low angles becomes larger than the period of modulations in the data. The inability to reproduce the data in this range suggests that the actual functional form for the angle averaging at these angles was more complicated than the assumed model.

The model-independent analysis was conducted as described for the *ex situ* case, except now the electric field intensities used were calculated using the reflection at the water-TiO_2 interface (i.e., using R_2, v_2, and E_2 for that interface). The incident E-field amplitude (E_2) above the water-TiO_2 interface was based on transmission of incident x-rays through a water equivalent thickness parameter (Table II) included in the fit, which accounted for the attenuation of the incident beam through the water and Kapton layers. The attenuation of the XSW over the thickness of the TiO_2 layer was, however, neglected as stated previously. During the model-independent analysis, the yield data was initially plotted as Y vs Q_{H_2O}, where Q_{H_2O} is the momentum transfer inside the aqueous layer. The data was then divided into segments of width $\Delta Q_{H_2O}=0.01$ Å^{-1} and the model-independent approach was used to obtain an amplitude and a phase for each segment. These model-independently derived

A and P values are plotted vs Q_{air} (referred as Q) in Fig. 6 (blue squares) for a direct comparison with the *ex situ* data. The model-independent phases are similar to the *ex situ* results, implying that the center position of the Ti layer should be comparable for the two samples. The derived amplitudes on the other hand, while similar to *ex situ* case in terms of their variation with Q in the study range, differ quite clearly in terms of their magnitude. Note in particular that the extrapolated value of $A_{Q=0}$ (i.e., the coherent fraction) is ~0.60 compared to the value of 0.86 observed for the *ex situ* data. The Fourier-inverted density profile for the *in situ* data [Fig. 5(B), dashed blue line] was obtained using $Q_2=Q_{H_2O}$ in Eq. (18) with the derived A and P values. This density profile is comparable to the *ex situ* case [Fig. 5(A)], showing that the formalism can be used to measure the *in situ* elemental distribution.

A model-based analysis shows good agreement with the model-independent results, both in terms of the A and P variation (Fig. 6, dashed blue lines), and the Ti profile [Fig. 5(B), solid blue line]. The center of the Ti distribution is 10.5 ± 1 Å below the surface and is within error of the value derived with model-independent approach (10.0 Å). It is comparable to (but somewhat larger than) the value from the *in situ* reflectivity analysis (7.5 Å). The width of the Ti layer, 20 ± 3 Å, is comparable to the reflectivity measurement (14.9 ± 0.2 Å). The structural parameters of the Ti layer for the *in situ* measurement are within error the same as that obtained for the *ex situ* results (Table II).

V. DISCUSSION

We have demonstrated that this model-independent formalism can be used to extract elemental Fourier amplitudes and phases from experimentally measured long-period x-ray standing wave data to directly obtain the elemental profiles from the fluorescence yield data. It has also been shown that the formalism can be applied to measure *in situ* distributions by imaging the Ti layer under a thin solution layer. The capability of imaging under aqueous media and with long-period XSW can be very valuable in measuring extended structures such as the diffuse double layer[39] at liquid-solid interfaces.

One significant factor in interpreting these data is the experimental resolution. The width of the profiles extracted with this approach does not reflect the intrinsic width of the distribution if the intrinsic width is smaller than the experimental resolution. This is the case for the Ti profiles in Fig. 5, where the model-independent profiles derived from the XSW data have a width of about 30 Å. The experimental resolution is given approximately by $\pi/(Q_{max}-Q_{min})$, where Q_{max} (Q_{min}) is the higher (lower) end of the fluorescence yield data range. Based on the Q ranges shown in Fig. 4(C), the spatial resolution of the XSW results can be estimated as ~33 Å for the *ex situ* data and ~45 Å for the *in situ* data. The resolution can be improved by measuring the data to a higher Q. (For example, a Q range of *beyond* 0.2 $Å^{-1}$, i.e., almost double the current data range of the fluorescence yield data, would be necessary for the analysis to resolve the intrinsic ~15-Å width and ultimately the vertical shape of the titania layer). However, the reduction in reflectivity with increasing Q decreases the fluorescence yield modulations, thus requiring longer counting times to obtain the necessary statistical significance.

The model-independent elemental Fourier amplitudes in Fig. 6(A) revealed a significant incoherent fraction for the *ex situ* measurements and an even greater incoherent fraction for the *in situ* measurements. We propose that this incoherency is primarily induced by diffusely or incoherently scattered x-rays that are produced by the incident and reflected beams passing through the layers of surrounding media. Since these secondary scattered x-rays are incoherent, their induced Ti $K\alpha$ XRF yield will show no interference effect. This gives rise to a background fluorescence signal that is added to the XSW-induced signal. Even though (for reasons of convenience) we use a secondary broad Ti distribution to mimic this incoherency effect in our model fits to the XSW data, it should be clear that the observed incoherency is due to an x-ray incoherency. This conclusion is supported by the observation that there is an increase in the incoherent fraction observed for the *in situ* XSW measurements compared to the *ex situ* measurements, since the Kapton and solution layers serve as additional sources of diffuse or incoherent scattering. When these different incoherent fractions are used in the model-dependent analyses for the two conditions (i.e., *ex situ* and *in situ*), the Ti profile parameters obtained are the same within experimental uncertainties.

The formalism described here is valid for an XSW generated by reflection from an interface. It can therefore be used for various geometries including TER and PML, and can also be extended for the single-crystal Bragg-XSW case. Note however, that while Parratt's formalism can be used to obtain the reflection coefficients needed in the analysis (R and ν) for the TER and PML regimes, as done in this paper, for the high-angle Bragg case these should be calculated using the precise dynamical diffraction theory for single crystals.[40] The current formalism can be compared to the previous model-independent approach that is applicable to the Bragg XSW case. In that case, the fluorescence yield measured around Hth order diffraction revealed the discrete amplitude and phase of the Hth *-order* Fourier-coefficient of the three-dimensional density distribution. Because of this, the sampling of the element-specific structure factor was limited to points in reciprocal space that satisfy the Bragg diffraction condition (and hence the modulo-d ambiguity was present). However with the current approach, the Fourier coefficients can be sampled at a substantially higher frequency through TER and PML XSW measurements, or even along the crystal truncation rods that pass through each Bragg diffraction condition. The sampling interval in this approach is only determined by the segment width chosen in the analysis which should be large enough so that the derived parameters are well defined. Because of the finer sampling, a unique reconstruction of more extended distributions becomes possible.

While the earlier and simpler formalism developed by Bedzyk[24] is also applicable for the reflection generated XSW, it is limited (in its current form) to the TER region of the data due to an assumption about the phase of the reflected wave. The present approach however places no constraints

on either the magnitude or phase of the reflected wave and is valid even beyond the TER region. This means that there are no constraints on the type of layered structure that is used to generate the standing waves, unlike the requirement of single crystals for Bragg-XSW case. Another distinguishing feature about the current approach is that it is applicable to XSW produced in an absorbing medium.

In the analysis shown in Secs. IV B and IV C, it was assumed that the elemental structure factor amplitude and phase are constant over the segment width ΔQ. This however induces some errors since the variation in A and P may not always be negligible. We now estimate the errors (in A and P) for the case of an elemental profile represented by a single Gaussian layer centered at a height z_0 above the surface with width σ, over the range of data in the segment ΔQ centered around Q_0. The amplitude and phase of the profile is given by $A(Q)=\exp(-\frac{1}{2}\sigma^2Q^2)$ and $P(Q)=\frac{1}{2\pi}QZ_0$. The change in A and P over the interval ΔQ, evaluated at $Q=Q_0$, can thus be written as, $\Delta A=\frac{dA}{dQ}\Delta Q=\{-Q\sigma^2\exp(-\frac{1}{2}\sigma^2Q^2)\}\Delta Q$, and $\Delta P=\frac{dP}{dQ}\Delta Q=\frac{1}{2\pi}Z_0\Delta Q$; and the fractional changes will be, $\frac{\Delta A}{A}=-Q\sigma^2\Delta Q$, and $\frac{\Delta P}{P}=\frac{\Delta Q}{Q}$. This suggests that if a constant segment width ΔQ is used in the analysis to divide the entire range of data for the case of a Gaussian distribution, the fractional error in phase due to the neglected change over the interval ΔQ will be larger at small Q while the errors in amplitude will be larger at higher Q depending on the width σ. Consider an example of a Gaussian profile having a width of $\sigma=5$ Å and sampled with a segment width, $\Delta Q=0.01$ Å^{-1}. At $Q=0.05$ Å^{-1}, the change in phase over ΔQ will be 20% while the change in amplitude will be 1%. Choosing a variable segment width ΔQ through the range of the data can help in reducing these errors.

In cases where the elemental structure factor changes rapidly or nonlinearly with Q, it may be important to include the gradient terms in the analysis, i.e., using four parameters A, P, dA/dQ, and dP/dQ for each segment ΔQ. These terms are particularly important for distributions that have multiple layers, as interference between the different layers can result in sharp changes in the variation in A and P as a function of Q. Since some degree of distortion will be induced in the results because of the nonlinear variations in the elemental structure factor over the region ΔQ, precise structural results will still be best obtained from a conventional model analysis, using the model-independent results as the basis for building the model. If necessary, additional parameters describing the higher-order changes can be included. It may also be beneficial to select smaller segment widths when the A and P variation is significant, although this may ultimately be limited by the sampling intervals of the experimental data.

VI. SUMMARY

We described a model-independent approach for directly obtaining elemental distribution profiles from multilayer structures by using x-ray fluorescence yield data for the case of reflection generated x-ray standing waves. The approach has been demonstrated by retrieving the Ti profile from the yield data measured both in air and under aqueous conditions. A distinguishing feature about the approach is that it allows determination of Fourier coefficients of the elemental profile at a more continuous sampling interval (in Q) than the previous model-independent approach that was applicable to Bragg-XSW where sampling was limited to Bragg diffraction condition. This finer Q sampling enables unique measurements of structures further away from the reflecting surface. Another uniqueness of the approach is that it makes no assumptions about the magnitude or phase of the reflected wave, and is therefore valid for any case of XSW generated through specular reflection from a multilayer structure, including periodic multilayers. The formalism can be used to extract not only the amplitudes and phases (of the elemental structure factor) but also their first or higher-order gradients, making it potentially useful in directly measuring complex profiles (such as multilayered distributions) where structure factor changes with Q can be complicated. Applicability to *in situ* systems makes the technique useful in imaging element profiles at liquid-solid interfaces, such as the adsorbed ion profile at aqueous-mineral interfaces. Since the technique allows analysis of the long-period standing waves data, it can also be used to image extended or diffuse elemental distributions.

ACKNOWLEDGMENTS

This work was supported by the U. S. Department of Energy (DOE), Office of Basic Energy Sciences, Division of Chemical Sciences, Geosciences, and Biosciences, through the project "Nanoscale Complexity at the Oxide-Water Interface" (Grant No. ERKCC41) at Oak Ridge National Laboratory. The data reported in this paper were collected at beamline 33BM-C at the Advanced Photon Source (APS), Argonne National laboratory. Initial measurements toward this effort were conducted at beamlines 6ID-B and 11ID-D. Use of the APS was also supported by the U.S. DOE, Office of Science, Office of Basic Energy Sciences. We are grateful to Chian Liu for growing the sputter deposited layers, Joe Libera and Jeffrey Elam for the ALD coating, Mike Wieczorek for dicing the Si wafer, and APS Sector 33 staff Jenia Karapetrova and Zhan Zhang for technical support.

[1] B. W. Batterman, Phys. Rev. Lett. **22**, 703 (1969).
[2] J. A. Golovchenko, B. W. Batterman, and W. L. Brown, Phys. Rev. B **10**, 4239 (1974).
[3] S. K. Andersen, J. A. Golovchenko, and G. Mair, Phys. Rev. Lett. **37**, 1141 (1976).
[4] Y. Qian, N. C. Sturchio, R. P. Chiarello, P. F. Lyman, T.-L. Lee, and M. J. Bedzyk, Science **265**, 1555 (1994).
[5] L. Cheng, P. Fenter, N. C. Sturchio, Z. Zhong, and M. J. Bedzyk, Geochim. Cosmochim. Acta **63**, 3153 (1999).
[6] J. Zegenhagen, Surf. Sci. Rep. **18**, 199 (1993).

[7] D. P. Woodruff, B. C. C. Cowie, and A. R. H. F. Ettema, J. Phys.: Condens. Matter **6**, 10633 (1994).
[8] M. J. Bedzyk and G. Materlik, Phys. Rev. B **31**, 4110 (1985).
[9] J. A. Golovchenko, J. R. Patel, D. R. Kaplan, P. L. Cowan, and M. J. Bedzyk, Phys. Rev. Lett. **49**, 560 (1982).
[10] A. Kazimirov, L. X. Cao, G. Scherb, L. Cheng, M. J. Bedzyk, and J. Zegenhagen, Solid State Commun. **114**, 271 (2000).
[11] T. W. Barbee, Jr. and W. K. Warburton, Mater. Lett. **3**, 17 (1984).
[12] M. J. Bedzyk, D. W. Bilderback, J. H. White, M. G. Bommarito, and H. D. Abruna, J. Electrochem. Soc. **134**, C132 (1987).
[13] M. J. Bedzyk, D. H. Bilderback, G. M. Bommarito, M. Caffrey, and J. S. Schildkraut, Science **241**, 1788 (1988).
[14] J. A. Libera, R. W. Gurney, C. Schwartz, H. Jin, T. L. Lee, S. T. Nguyen, J. T. Hupp, and M. J. Bedzyk, J. Phys. Chem. B **109**, 1441 (2005).
[15] P. L. Cowan, J. A. Golovchenko, and M. F. Robbins, Phys. Rev. Lett. **44**, 1680 (1980).
[16] P. Fenter, L. Cheng, S. Rihs, M. L. Machesky, M. J. Bedzyk, and N. C. Sturchio, J. Colloid Interface Sci. **225**, 154 (2000).
[17] Z. Zhang, P. Fenter, L. Cheng, N. C. Sturchio, M. J. Bedzyk, M. Předota, A. Bandura, J. D. Kubicki, S. N. Lvov, P. T. Cummings, A. A. Chialvo, M. K. Ridley, P. Bénézeth, L. Anovitz, D. A. Palmer, M. L. Machesky, and D. J. Wesolowski, Langmuir **20**, 4954 (2004).
[18] M. J. Bedzyk and G. Materlik, Phys. Rev. B **32**, 6456 (1985).
[19] L. Cheng, P. Fenter, M. J. Bedzyk, and N. C. Sturchio, Phys. Rev. Lett. **90**, 255503 (2003).
[20] N. Hertel, G. Materlik, and J. Zegenhagen, Z. Phys. B: Condens. Matter **58**, 199 (1985).
[21] M. J. Bedzyk and L. Cheng, in *Reviews in Mineralogy and Geochemistry*, edited by P. Fenter, M. L. Rivers, N. C. Sturchio, and S. R. Sutton, (The Mineralogical Society of America, Washington, DC, USA 2002), p. 221.
[22] M. J. Bedzyk, G. M. Bommarito, and J. S. Schildkraut, Phys. Rev. Lett. **62**, 1376 (1989).
[23] A. S. Templeton, T. P. Trainor, S. J. Traina, A. M. Spormann, and G. E. Brown, Jr., Proc. Natl. Acad. Sci. U.S.A. **98**, 11897 (2001).
[24] M. Bedzyk, in *The X-Ray Standing Wave Technique: Principles and Applications*, Series on Synchrotron Radiation Techniques and Applications Vol. 7, edited by Jorg Zegenhagen and Alexander Kazimirov (World Scientific, Singapore, in press).
[25] J. B. Kortright and A. Fischer-Colbrie, J. Appl. Phys. **61**, 1130 (1987).
[26] J. C. Lin, J. A. Kellar, J. H. Kim, N. L. Yoder, K. H. Bevan, S. T. Nguyen, M. C. Hersam, and M. J. Bedzyk, Eur. Phys. J. Spec. Top. **167**, 33 (2009).
[27] A. A. Escuadro, D. M. Goodner, J. S. Okasinski, and M. J. Bedzyk, Phys. Rev. B **70**, 235416 (2004).
[28] C.-Y. Kim, J. W. Elam, M. J. Pellin, D. K. Goswami, S. T. Christensen, M. C. Hersam, P. C. Stair, and M. J. Bedzyk, J. Phys. Chem. B **110**, 12616 (2006).
[29] Z. Zhang, P. Fenter, L. Cheng, N. C. Sturchio, M. J. Bedzyk, M. L. Machesky, and D. J. Wesolowski, Surf. Sci. **554**, L95 (2004).
[30] J. Als-Nielsen and D. McMorrow, *Elements of Modern X-Ray Physics* (Wiley, New York, 2001).
[31] L. G. Parratt, Phys. Rev. **95**, 359 (1954).
[32] M. Leskelä and M. Ritala, Angew. Chem., Int. Ed. **42**, 5548 (2003).
[33] J. A. Libera, Ph.D. thesis, Northwestern University, 2005.
[34] D. A. Walko, D. A. Arms, and E. C. Landahl, J. Synchrotron Radat. **15**, 612 (2008).
[35] Z. Zhang, Ph.D. thesis, Northwestern University, 2004.
[36] D. K. G. de Boer, Phys. Rev. B **44**, 498 (1991).
[37] S. K. Ghose and B. N. Dev, Phys. Rev. B **63**, 245409 (2001).
[38] G. M. Bommarito, Ph.D. thesis, Cornell University, 1992.
[39] J. N. Israelachvili and G. E. Adams, J. Chem. Soc., Faraday Trans. 1 **74**, 975 (1978).
[40] B. W. Batterman and H. Cole, Rev. Mod. Phys. **36**, 681 (1964).